Why Ammoniated Lithium Borohydrides Liquefy and Resolidify?

Qian Wang[1†], Zixin Xu[2†], Ryuhei Sato[3], Hiroki Miyaoka[4], Takayuki Ichikawa[2], Eric Jianfeng Cheng[1], Shin-ichi Orimo[1,5], Fangqin Guo[2,*], Hao Li[1,*]

[1] Advanced Institute for Materials Research (WPI-AIMR), Tohoku University, Sendai 980–8577, Japan

[2] Graduate School of Advanced Science and Engineering, Hiroshima University, 1-4-1 Kagamiyama, Higashi-Hiroshima 739-8527, Japan

[3] Department of Materials Engineering, The University of Tokyo, 7-3-1 Hongo, Bunkyo-ku, Tokyo 113-8656, Japan

[4] Core Facility Management Center, Hiroshima University, 1-3-1 Kagamiyama, Higashi-Hiroshima, 739-8530, Japan

[5] Institute for Materials Research (IMR), Tohoku University, Sendai 980–8577, Japan

[†] Equal contributions

* Corresponding authors, E-mails: fang-qin-guo@hiroshima-u.ac.jp (F.G.), li.hao.b8@tohoku.ac.jp (H.L.)

Abstract

Ammonia (NH_3) absorption drives $LiBH_4 \cdot xNH_3$ through a re-entrant "solid–liquid–solid" transition: **$LiBH_4 \cdot NH_3$ is a well-defined solid ammoniate, compositions near $LiBH_4 \cdot 2NH_3$ are liquid-like or partially liquefied, whereas $LiBH_4 \cdot 3NH_3$ returns to a more rigid non-liquid ammoniate state.** However, the microscopic origin of this unintuitive response remains a long-lasting mystery. Here, we uncover its mechanism. Cross-database analysis identifies borohydrides as a particularly state-diverse and composition-responsive material family. Structure prediction and *ab initio* molecular simulations reveal that NH_3 progressively replaces BH_4^- in the Li coordination shell. The liquid-like state emerges not at the highest NH_3 loading but near $x \approx 2$, where Li–N and Li–B coordination modes are strongly mixed, coordination memory is weakest, and the sampled Li–N/N···B coordination landscape is broadest. Further ammoniation produces Li–N-dominant coordination and slows BH_4^-/NH_3 contact renewal, with the resulting increase in network persistence and accompanying recovery of a rigid ammoniate state. Pressure–composition isotherm, ^1H and ^{11}B nuclear magnetic resonance, and Raman measurements support this non-monotonic state evolution and associated BH_4^-/NH_3 reorganization. These findings transform ammonia-induced liquefaction from an empirical phase anomaly into a competition between native-network disruption, mixed-coordination frustration, and ligand-built network reconstruction, providing a framework for chemically switching between transport-favouring fluidity and stability-favouring rigidity in hydrogen-rich materials.

INTRODUCTION

Complex hydrides constitute a versatile family of hydrogen-rich materials relevant to hydrogen and ammonia storage, electrochemical energy storage, and related energy-conversion processes.[1, 2, 3] Their appeal arises from their high gravimetric and volumetric hydrogen densities and from the structural and dynamical flexibility of complex anions.[4] However, their performance is often constrained by slow transport through rigid condensed phases, insufficient reactant contact, and interfacial resistance.[5, 6] Physical state is therefore an important yet underdeveloped design variable: liquid-like phases can enhance mass transport and wetting, whereas solids provide dimensional and mechanical stability.[3] Hydrogen-rich liquids formed from complex hydrides further demonstrate the potential of deliberately controlling hydride phase state.[7] Controlled switching between fluidity and rigidity could thus reconcile fast transport with structural robustness, but the microscopic principles governing such switching remain poorly understood.

Borohydrides are particularly suitable for examining this problem because the BH_4^- anion combines high hydrogen content with rotational dynamics and adaptable cation coordination. $LiBH_4$ has a high theoretical hydrogen capacity of 18.5 wt%,[8, 9] while borohydride- and *closo*-borate-based electrolytes can reach Li^+ or Na^+ conductivities of 10^{-3}–10^{-2} S cm^{-1} when anion rotation, substitution, disordering, or molecular-complex formation is activated.[10, 11, 12] Borohydrides can also reversibly absorb NH_3 at high density,[13, 14] while $LiBH_4$ and $NaBH_4$ can form low-viscosity liquid ammoniate phases under certain conditions.[15] In these materials, NH_3 acts not only as a stored molecule but also as a ligand that competes with BH_4^- for cation coordination and reorganizes network connectivity, molecular mobility, and macroscopic material state.

$LiBH_4{\cdot}xNH_3$ provides a striking example of composition-driven re-entrant behavior.[13, 16, 17, 18] Notably, their physical states change **non-monotonically** with NH_3 content: **$LiBH_4{\cdot}NH_3$ is a well-defined solid ammoniate, the compositions near $LiBH_4{\cdot}2NH_3$ are liquid-like or partially liquefied, whereas $LiBH_4{\cdot}3NH_3$ returns to a more rigid ammoniate state.**[13, 15, 19] Early

pressure-composition-temperature (PCT) measurements revealed a strongly composition-dependent phase diagram, with distinct phase fields around $x \approx 0.5$, 1, 2, 3, and 4 and lower liquidus temperatures across several intervening composition ranges.[19] The structure and melting behavior of $LiBH_4 \cdot 0.5NH_3$ provide a well-defined low-NH_3 reference state,[12] while compositions within reported two-phase regions represent phase coexistence rather than unique single phases. Nevertheless, these macroscopic phase relationships do not explain why initial NH_3 uptake disrupts the solid structure whereas further ammoniation restores rigidity. The liquid-like nature of $LiBH_4 \cdot 2NH_3$ also complicates direct determination of its local structure by conventional crystallography, leaving the atomistic origin of this re-entrant transition unresolved.

Here, we investigate the structural and dynamical origin of NH_3-dependent "solid–liquid–solid" evolution in $LiBH_4 \cdot xNH_3$ (x = 0.5, 1, 2, 3, and 4). Artificial intelligence (AI) agent-assisted cross-database analysis is combined with structure prediction, finite-temperature molecular dynamics, enhanced sampling, and experimental measurements. To the best of our knowledge, this work provides the first mechanistic explanation of this long-standing phenomenon. NH_3 progressively replaces BH_4^- in the Li coordination shell, but the liquid-like state emerges specifically near $x \approx 2$, where Li–N and Li–B coordination modes are strongly mixed and coordination memory is weakest. Further ammoniation produces Li–N-dominant coordination and a more persistent BH_4^-/NH_3 network, increasing network persistence and restoring rigidity. These results identify the interplay between coordination-shell mixing and network persistence as the microscopic origin of the re-entrant transition and provide a potentially transferable framework for understanding transient fluidity in other complex hydrides.

Results and Discussion

Cross-database analysis of ammonia-induced state diversity

Due to the limited available NH_3-storage dataset for hydrides, comprising approximately 12 studies[15, 19, 20, 21, 22, 23, 24, 25, 26, 27, 28, 29] and 36 materials in the present collection, related hydride records

from our recently developed Digital Battery platform (*DigBat*)[30] and Digital Hydrogen platform (*DigHyd*)[31] were also included as complementary references rather than as direct measures of material state (**Fig. 1a**). *DigBat* contains ~2,000 experimental data entries of >200 hydride electrolytes, while *DigHyd* comprises >30,000 hydride-related data entries. Within the ammonia storage dataset, liquid and solid–liquid coexistence states are concentrated primarily in ammonia borane and borohydrides, whereas NH_3-loaded metal halides are reported predominantly as solids (**Fig. 1b**). Borohydrides exhibit the broadest state diversity, spanning solid, liquid, and composition-dependent or transitional states. This contrast demonstrates that NH_3 incorporation alone is insufficient to induce liquefaction. **Instead, the resulting physical state likely depends on how NH_3 disrupts the original intermolecular or anion-supported network and whether a new persistent coordination network is subsequently established.**

DigBat and *DigHyd* were then used to examine whether related BH_4^-/NH_3 materials show composition- and cation-dependent responses (**Fig. 1c**). In *DigBat*, the ionic conductivities of solid electrolytes were compared near 310 K. The $LiBH_4$-based series is limited to NH_3/BH_4 = 0, 0.5, and 1, corresponding to $LiBH_4$, $LiBH_4{\cdot}0.5NH_3$, and $LiBH_4{\cdot}NH_3$, and its conductivity increases with increasing NH_3/BH_4 ratio. Higher-loading $LiBH_4{\cdot}2NH_3$, $LiBH_4{\cdot}3NH_3$, and $LiBH_4{\cdot}4NH_3$ are not included in these solid electrolyte structural/property records because they correspond to liquid-like, partially liquefied, or structurally unresolved regimes. In contrast to the monotonic Li-based trend, the $Mg(BH_4)_2$-based series shows a non-monotonic response, reaching a maximum conductivity of approximately 5×10^{-7} S cm^{-1} near NH_3/BH_4 = 0.9 and then decreasing at higher NH_3 content.[32]

In *DigHyd*, the hydrogen desorption capacities of Mg-, Mn-, and V-containing borohydrides tend to increase with NH_3/BH_4 ratio under different conditions. Together with the ammonia storage records, **these trends identify the NH_3/BH_4 ratio as a key compositional variable governing material-state and property responses, while showing that the direction and magnitude of these responses depend on cation identity and the measured property.** AI agent-assisted descriptor

screening across the three datasets further highlighted coordination-related variables as informative descriptors (**Figs. S1–S4** and **Supplementary Videos 1-2**).

This observation motivated a focused analysis of the Li^+ coordination environment in $LiBH_4{\cdot}xNH_3$, where the cation identity remains fixed while the NH_3/BH_4 ratio varies. Experimentally reported structures were used for $LiBH_4{\cdot}0.5NH_3$ and $LiBH_4{\cdot}NH_3$, whereas candidate structures for $LiBH_4{\cdot}2NH_3$, $LiBH_4{\cdot}3NH_3$, and $LiBH_4{\cdot}4NH_3$ were obtained from USPEX[33] structure searches based on genetic algorithm (**Figs. S5-S9**). Representative structures show a progressive change in the Li coordination environment (**Fig. 1d**): Li^+ is coordinated predominantly by BH_4^- at low x, mixed Li–N and Li–B contacts emerge at intermediate x, and Li–N coordination becomes dominant at higher x. This qualitative progression was subsequently quantified through Li-shell composition, coordination exchange, and BH_4^-/NH_3 network connectivity.

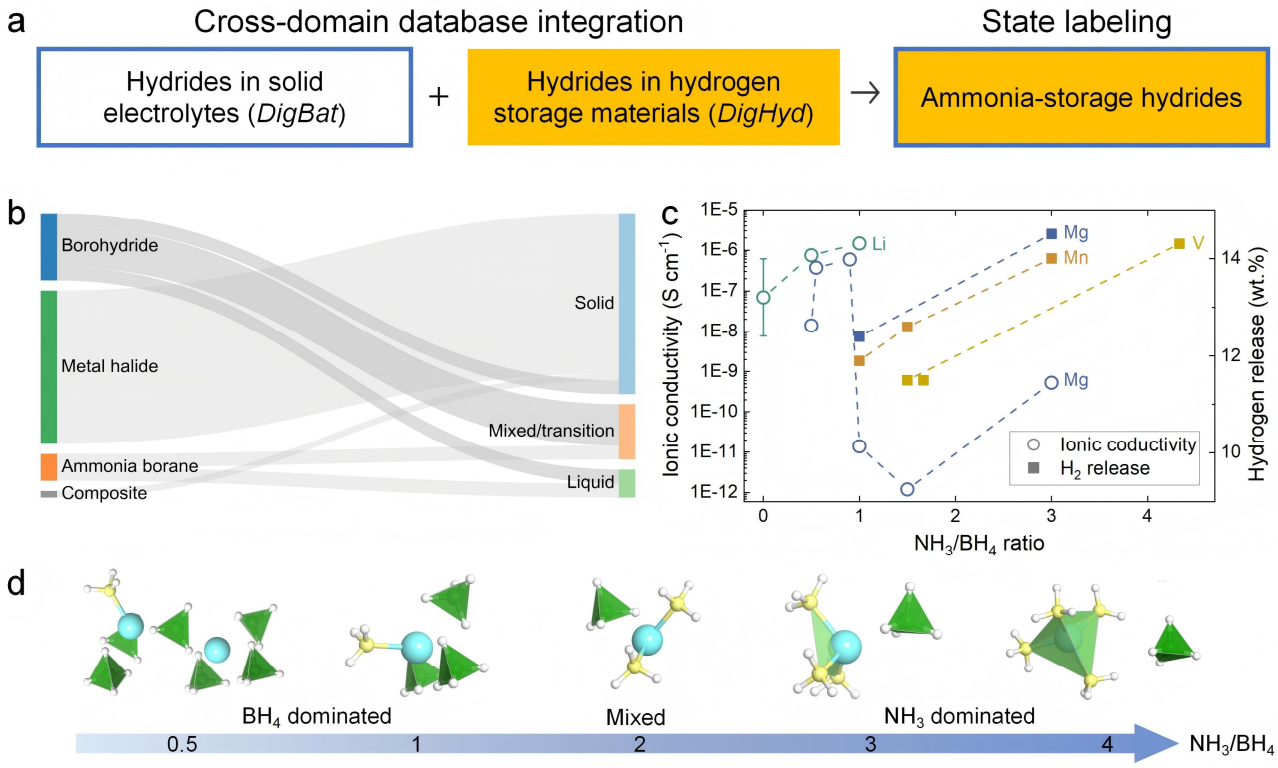

Fig. 1. Cross-database patterns in ammonia-induced state and property evolution. a, Complementary data domains for ammonia-induced state anomalies. **b**, Reported physical-state distribution of ammonia-storage borohydrides, metal halides, ammonia boranes, and composites. **c**, Ionic conductivity and hydrogen desorption capacity as functions of NH_3/BH_4 ratio for related borohydride materials from *DigBat* and *DigHyd* databases, respectively. **d**, Representative Li

coordination environments in $LiBH_4 \cdot xNH_3$ with increasing x loading; cyan, green, yellow, and white spheres represent Li, B, N, and H atoms, respectively.

Li coordination-shell switching defines a mixed-shell regime

Before examining the finite-temperature coordination dynamics, the relative 0 K stability of the candidate structures was evaluated. The corresponding 0 K electronic-energy convex hull places the x = 1, 3, and 4 compositions on the hull, whereas x = 0.5 and x = 2 lie 1.34 and 11.49 meV atom^{-1} above it, respectively (**Fig. S10**).

Unbiased *ab initio* molecular dynamics simulations were used to quantify how NH_3 uptake changes the local Li environment in $LiBH_4 \cdot xNH_3$ after structural equilibration. First-shell Li–N and Li–B coordination numbers (CN) were defined from radial distribution functions (RDF) using consistent cutoffs across the composition series (**Fig. S11**). Li–N coordination describes the occupation of the Li shell by NH_3 molecules, whereas Li–B coordination shows the proximity of BH_4^- units to the same local environment.

RDF analysis shows a clear substitution of the Li coordination shell with increasing NH_3 loading. Li–N correlations exhibit a pronounced first-shell peak near 2 Å for all $LiBH_4 \cdot xNH_3$ compositions, and the first-shell contribution increases with x (**Fig. 2a**). In contrast, the Li–B first-shell correlations decrease and broaden with increasing NH_3 loading (**Fig. 2b**). The corresponding neighbor statistics confirm this opposite trend: CN(Li–N) increases, whereas CN(Li–B) decreases (**Fig. 2c**). The two contributions are most comparable at x = 2, whereas Li–N coordination becomes dominant by x = 3. $LiBH_4 \cdot 2NH_3$ therefore represents a mixed-coordination regime near the crossover from BH_4^--rich to NH_3-rich Li environments.

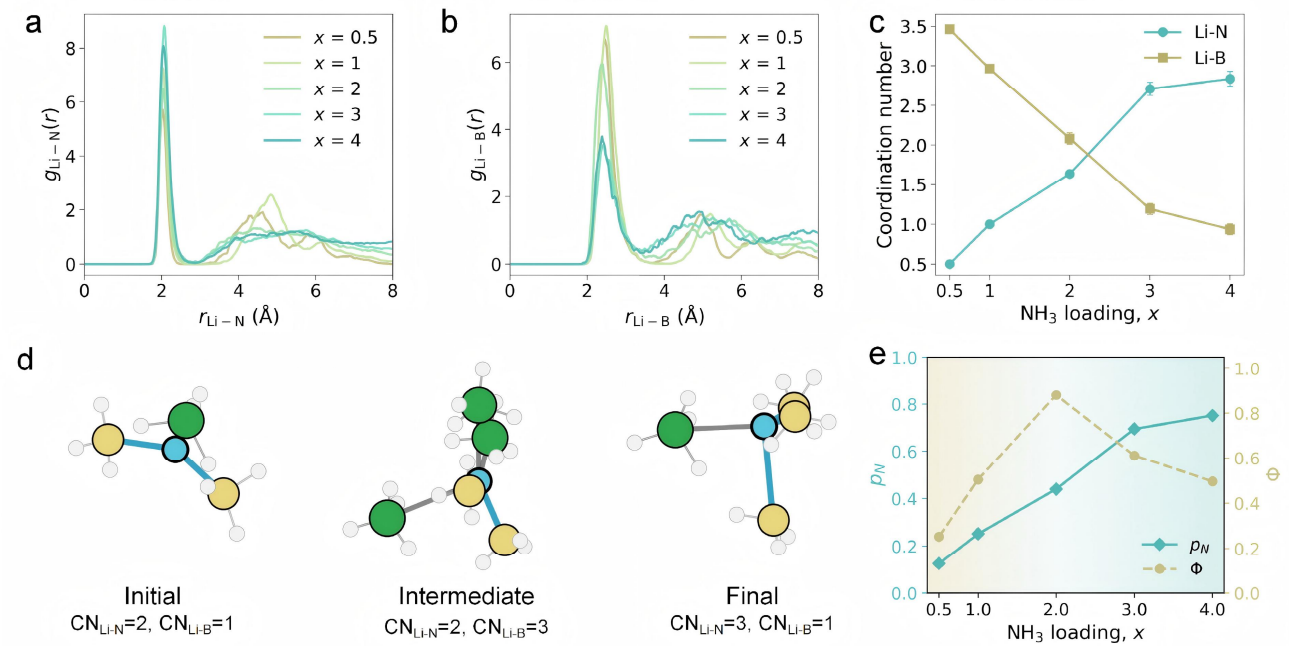

Fig. 2. Li coordination-shell switching in $LiBH_4 \cdot xNH_3$. **a**,**b**, Li–N (**a**) and Li–B (**b**) radial distribution functions (RDFs) for different x. **c**, First-shell Li–N and Li–B coordination numbers as function of NH_3 loading. **d**, Representative local configurations from an unbiased *ab initio* molecular dynamics trajectory of $LiBH_4 \cdot 2NH_3$; cyan, green, yellow, and white spheres denote Li, B, N, and H atoms, respectively. **e**, NH_3 fraction in the Li coordination shell, p_N, and normalized shell-mixing entropy, Φ, as a function of NH_3 loading.

Representative configurations from the $LiBH_4 \cdot 2NH_3$ trajectory illustrate this mixed-shell regime (**Fig. 2d**). The joint Li–N/Li–B coordination distributions show the corresponding composition-dependent shift from BH_4^--rich to NH_3-rich environments, with $LiBH_4 \cdot 2NH_3$ occupying the most pronounced mixed-shell region (**Fig. S12**).

To quantify Li-shell composition and mixing, we defined the NH_3 fraction (p_N), and the normalized binary Shannon entropy of the Li-shell composition (Φ), hereafter referred to as the shell-mixing entropy:[34]

$$p_N = \frac{CN_{Li-N}}{CN_{Li-B}+CN_{Li-N}}, \Phi = -\frac{p_N \ln(p_N)+(1-p_N)\ln(1-p_N)}{ln2}.$$

Here, Φ is a dimensionless information-theoretic measure of shell mixing rather than a thermodynamic entropy. Φ = 0 for a single dominant shell component and Φ = 1 for equal Li–N and Li–B contributions. As shown in **Fig. 2e**, p_N increases monotonically with x, reflecting progressive replacement of BH_4^--associated Li^+ by NH_3. By contrast, Φ varies non-monotonically and reaches its

maximum at x = 2. Therefore, $LiBH_4 \cdot 2NH_3$ exhibits the highest Li-shell mixing among the compositions examined. This mixed-shell regime motivates the following *ab initio* metadynamics (MetaD) analysis of the coordination landscape.

Metadynamics (MetaD) simulations reveal non-monotonic broadening of the coordination landscape

Ab initio MetaD[35] was used to evaluate whether the mixed-shell regime identified near x = 2 corresponds to a broadened coordination space. The Li–N coordination variable measures the occupation of the Li^+ cation shell by NH_3, whereas the N···B network-contact variable describes the association between NH_3 and the surrounding BH_4^- framework. Li–B coordination largely mirrors the replacement of BH_4^- by NH_3 within the Li shell (**Fig. S13**); therefore, the N···B variable was selected to provide complementary information on network reorganization. At x = 1, the bias-derived coordination landscape is confined to a relatively localized region at high Li–N coordination and strong N···B network contact, consistent with a comparatively well-defined coupling between NH_3 coordination to Li^+ and the surrounding BH_4^- framework (**Fig. 3a**). At x = 2, the sampled region expands markedly, particularly along the Li–N coordination dimension, and covers the broadest coupled Li–N/N···B coordination region (**Fig. 3b**). Although x = 4 samples a comparable N···B range, it remains confined to a narrower Li–N-dominant region (**Fig. S14**). Internal pressures were comparable across compositions in both the unbiased and MetaD simulations, with no anomaly at x = 2, supporting their use for comparative analysis of local coordination dynamics (**Table S1**).

The time-dependent position of the dominant basin provides a complementary view of coordination-space migration during MetaD sampling (**Fig. 3c**). Low- and high-NH_3 compositions remain confined to narrower regions of the Li–N/N···B plane, whereas $LiBH_4 \cdot 2NH_3$ shows a larger displacement, indicating easier access to adjacent cation-shell and anion-framework configurations. The corresponding time-resolved collective-variable traces are shown in **Fig. S15**.

The expanded landscape was quantified by the 95% sampled region (A_{95}), and by the fluctuation

of the N···B network-contact coordinate (**Fig. 3d**). A_{95} reaches a maximum at $x = 2$, showing that the intermediate composition explores the broadest coordination region within the present sampling window. N···B fluctuations increase with NH_3 loading and remain substantial at higher x, indicating continued reorganization of the BH_4^-/NH_3 network. $LiBH_4{\cdot}2NH_3$ is therefore distinguished not by network fluctuations alone, but by their coexistence with the broadest coupled Li-shell/network landscape. Both metrics approach stable values during the late stage of the simulations (**Fig. S16**).

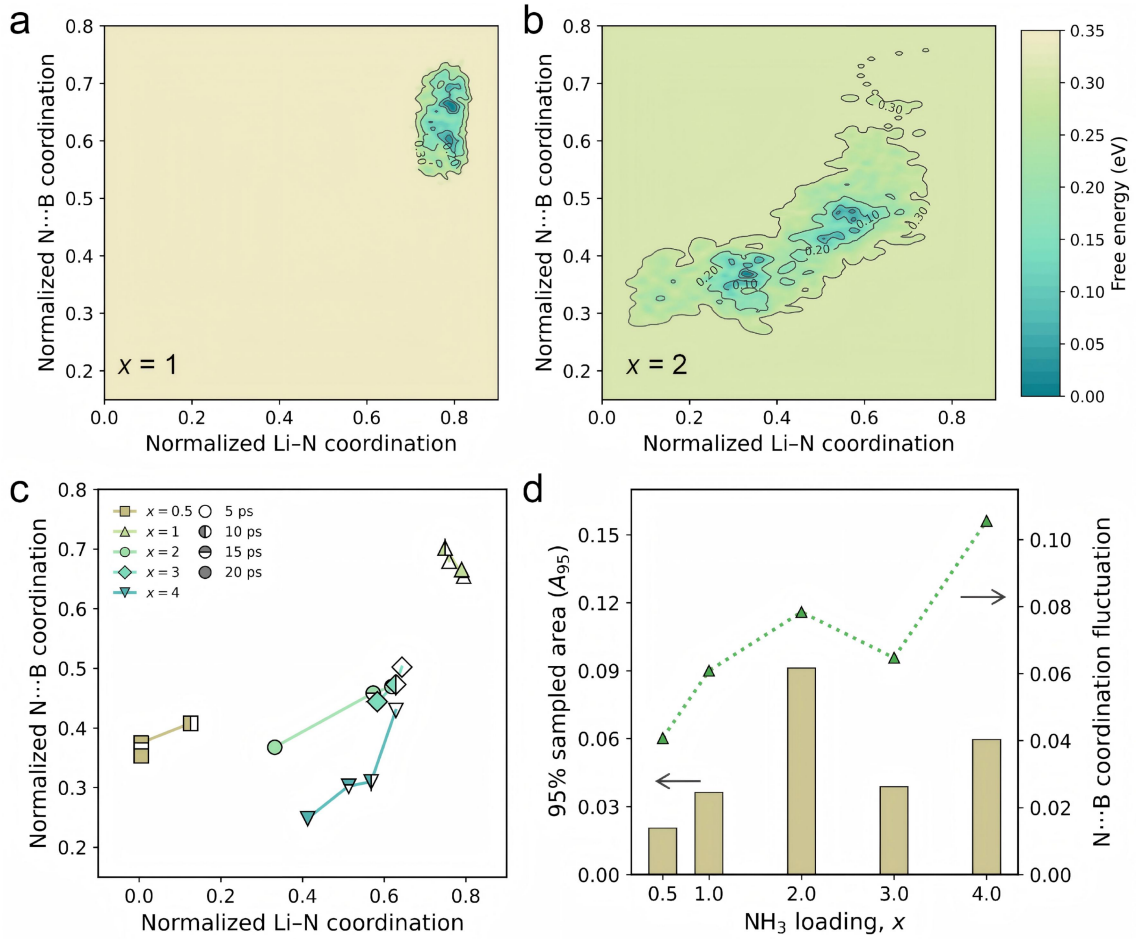

Fig. 3. MetaD exploration of coordination space in $LiBH_4{\cdot}xNH_3$. a, **b**, Bias-derived coordination landscapes at $x = 1$ (**a**) and $x = 2$ (**b**), projected onto the normalized Li–N coordination and N···B network-contact variables. **c**, Time evolution of the dominant-basin positions during MetaD sampling. **d**, Composition dependence of the area containing 95% of the sampled collective-variable points (A_{95}) and N···B network-contact fluctuation.

NH_3 loading first maximizes shell mixing and then increases the BH_4^-/NH_3 network persistence

The MetaD simulations indicate that Li-shell rearrangement is coupled to changes in the N···B network-contact variable. Unbiased trajectories were therefore analyzed to determine how NH_3

loading reorganizes the mixed BH_4^-/NH_3 network surrounding the Li coordination shell. BH_4^-/NH_3 network edges were defined using the first-shell N···B criterion (**Fig. S17**).

The N···B RDFs retain a pronounced first-shell peak across the full composition series, indicating persistent local association between NH_3 and BH_4^- (**Fig. 4a**). However, the first-shell N···B coordination number decreases with increasing x, consistent with the decreasing BH_4^-/NH_3 ratio as the NH_3 fraction increases (inset of **Fig. 4a**). This reduction in local coordination does not imply fragmentation of the contact network. The largest connected-component fraction (f_{LCC}) increases sharply with NH_3 loading and exceeds 0.9 near x = 2 (**Fig. 4b**), showing that the intermediate composition already contains an extended BH_4^-/NH_3 network (**Fig. S18**). Increasing NH_3 loading therefore produces a network that is less locally dense but more globally connected.

The temporal persistence of this network also changes with composition. The short-time edge-turnover rate (k_{turn}) decreases with increasing x and remains at lower values at x = 3 and x = 4 (**Figs. 4b** and **S19a**), consistent with slower decay of edge persistence at higher NH_3 loading (**Fig. S19b**). Low-x compositions therefore renew BH_4^-/NH_3 contacts more rapidly, whereas NH_3-rich compositions retain a larger fraction of their initial edges over the same lag time. Further increasing NH_3 loading consequently slows network renewal and increases the temporal persistence of the NH_3-rich contact network. Importantly, k_{turn} describes the replacement of N···B contact edges rather than bulk molecular mobility. The faster turnover at low x therefore reflects fluctuations within a sparse network, whereas x = 2 combines extensive connectivity with strong coordination-shell mixing and continued network reorganization.

The descriptor map in **Fig. 4c** summarizes the coupled response of the Li coordination shell and the surrounding BH_4^-/NH_3 network. The Li-shell NH_3 fraction, p_N, increases monotonically with NH_3 loading, whereas the shell-mixing entropy, Φ, reaches a maximum near x = 2. In parallel, the normalized N···B coordination number decreases, f_{LCC} increases and remains high beyond x = 2, and the normalized k_{turn} decreases at higher NH_3 loading. Thus, x = 2 combines maximal shell mixing

with an extended but dynamically renewing network, whereas x = 3 and 4 exhibit Li–N-dominant coordination together with slower network renewal. These trends identify x = 2 as a highly mixed and dynamically reconfigurable regime, consistent with enhanced configurational disorder and liquid-like mobility.

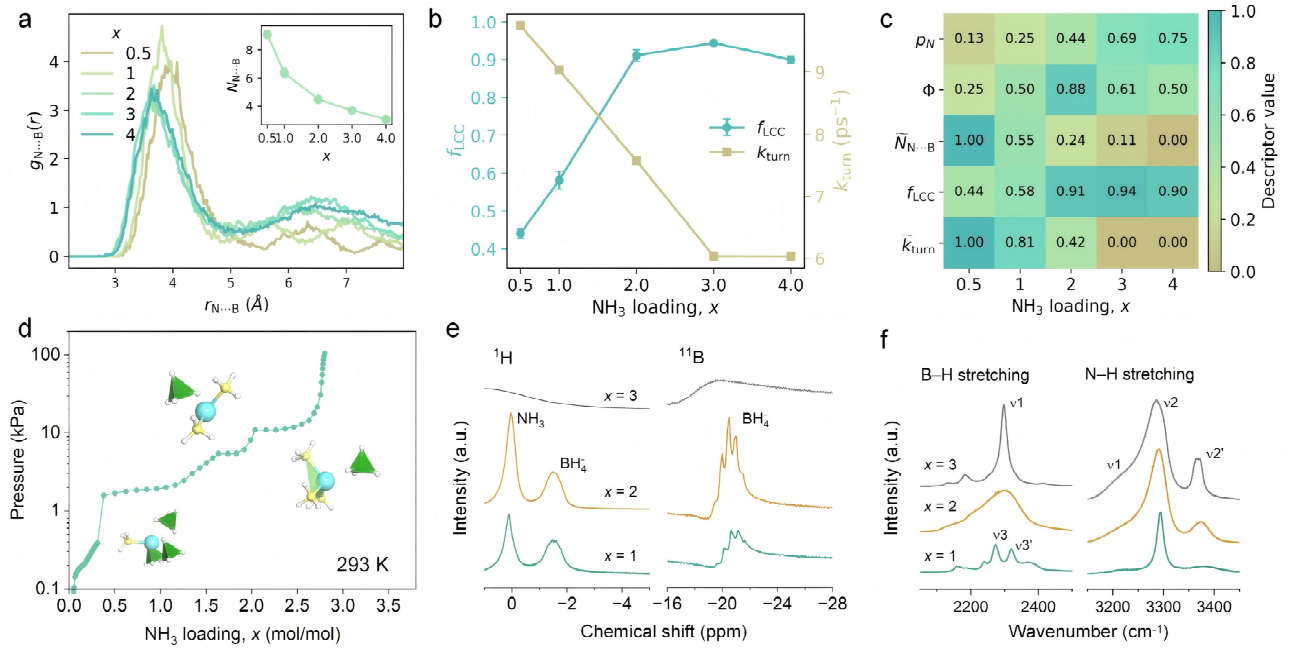

Fig. 4. BH_4^-/NH_3 network reorganization in $LiBH_4{\cdot}xNH_3$. **a**, N···B RDFs. Inset, first-shell N···B neighbor number versus NH_3 loading. **b**, NH_3-loading dependence of the largest connected-component fraction, f_{LCC}, and edge-turnover rate, k_{turn}. **c**, Descriptor map of p_N, Φ, $\widetilde{N}_{N\cdots B}$, f_{LCC}, and $\tilde{k}_{turn}$. The tilde denotes normalization across the investigated compositions. **d**, Pressure–composition isotherm for NH_3 absorption by $LiBH_4$. Inset, representative structures of $LiBH_4{\cdot}xNH_3$; cyan, green, yellow, and white spheres represent Li, B, N, and H atoms, respectively. **e**, ^{1}H and ^{11}B NMR spectra of $LiBH_4$ at increasing NH_3 absorption amount. **f**, Raman spectra of $LiBH_4$ during NH_3 absorption. **Panels d-f** were adapted from Ref.[15].

Room-temperature pressure–composition isotherm (PCI), nuclear magnetic resonance (NMR), and Raman measurements provide experimental tests of this composition-dependent sequence. At 293 K, the sequential formation of $LiBH_4{\cdot}NH_3$, $LiBH_4{\cdot}2NH_3$, and $LiBH_4{\cdot}3NH_3$ occurs at approximately 1.83, 5.40, and 10.8 kPa, with corresponding entropy changes of −106, −168, and −98.9 J mol^{-1} K^{-1}, respectively (**Fig. 4d**). The substantially larger magnitude of the entropy change for the x = 1→2 uptake step occurs in the same composition range as the maximum in Φ, consistent

with pronounced reorganization of the local Li coordination environment near $x \approx 2$. Together with the sloping PCI region between $x \approx 1.5$ and 2 and the reported partial liquefaction,[15, 16, 17, 18] these observations place the onset of the disordered intermediate near $x \approx 2$. Clear Li–N dominance is established only by $x = 3$, coinciding with the recovery of a more rigid and structurally defined ammoniate state.

The relatively sharp ^{1}H and ^{11}B resonances at $x \approx 2$ indicate motional narrowing and a liquid-like local environment, supporting reduced structural persistence and rapid local exchange in the mixed-shell regime (**Fig. 4e**). At $x \approx 3$, the strong attenuation or disappearance of these resonances is consistent with static broadening and the recovery of a rigid $LiBH_4 \cdot 3NH_3$ environment, in good agreement with Li–N-dominant coordination and slower BH_4^-/NH_3 network renewal. Upon formation of $LiBH_4 \cdot NH_3$, the B–H stretching band near 2298 cm^{-1} (ν1) is suppressed, whereas the band near 2274 cm^{-1} (ν3) and its adjacent shoulder (ν3') increase in intensity and shift in frequency (**Fig. 4f**). Continued evolution of the B–H and N–H regions from $x = 1$ to 3 further supports the reorganization of the local BH_4^- and NH_3 environments across the same coordination sequence. Taken together, these measurements support a re-entrant state response governed by the coupled evolution of Li-shell composition, coordination dynamics, and network persistence rather than a simple monotonic progression of NH_3 solvation. The liquid-like intermediate nevertheless retains substantial molecular character rather than behaving as a fully dissociated ionic solution, with intact BH_4^- and NH_3 participating in a dynamically reorganizing coordination network.

Discussion

The atomistic structures of $LiBH_4 \cdot 2NH_3$, $LiBH_4 \cdot 3NH_3$, and $LiBH_4 \cdot 4NH_3$ remain experimentally unresolved. Therefore, we employed USPEX crystal-structure searches to obtain low-energy, periodically ordered candidates that serve as structural reference states. The 0 K stability analysis places the liquid-like $x = 2$ composition above the tie line connecting the neighboring $x = 1$ and $x = 3$

ammoniates, indicating that its finite-temperature liquid-like behavior cannot be explained by static electronic energies alone. Despite the ordered starting structures, finite-temperature dynamics reveal the greatest degree of disorder at $x = 2$, while MetaD sampling identifies the broadest coupled coordination space at the same composition. The liquid-like tendency therefore emerges from dynamic access to competing local coordination environments rather than from an initially disordered structural model.

These discrete reference structures cannot, however, describe the full distribution of local environments within the experimentally reported intermediate composition ranges and two-phase fields. The two-phase fields represent macroscopic phase coexistence, while dynamically interconverting coordination motifs may also contribute within the constituent phases. Structural organization beyond the first Li coordination shell, including higher-order BH_4^-/NH_3 associations and longer-range packing, may further influence the precise state boundaries. The present models therefore establish systematic composition-dependent coordination trends, whereas the detailed structures of the liquid-like and coexisting phases await direct experimental resolution.

Composition-controlled state switching could decouple the fluidity required for transport or processing from the rigidity required during operation. In hydrogen-storage reactions, transient mobility may improve reactant contact and hydrogen transfer, while subsequent rigidification may suppress segregation and restore structural stability. More broadly, chemically induced transient fluidity may facilitate ion transport and interfacial contact in solid/liquid electrolyte systems and could provide a conceptual route to overcoming kinetic limitations during the formation of hydrogen-rich hydride phases. Related forms of dynamic hydride chemistry are already exploited in ammonia synthesis: metal-imide chemical looping separates nitrogen fixation from hydrogenation,[36] whereas ternary ruthenium complex hydrides couple hydridic hydrogen transfer to associative NH_3 formation.[37] In electrochemical manufacturing, electrolyte melt infiltration similarly exploits a liquid processing state followed by solidification to improve electrode filling and interfacial contact.[38] An

NH_3-responsive hydride could analogously provide fluidity for wetting and pore infiltration, followed by rigidification during operation. Practical use of $LiBH_4{\cdot}xNH_3$ would nevertheless require control of NH_3 volatility, electrochemical stability, interfacial compatibility, and cycling reversibility. Whether similar switching can be realized in ammonia-free hydrides through substitution, eutectic formation, defects, or nanoconfinement remains an important direction for future study.

Conclusion

In summary, we have identified the interesting mechanism of the long-lasting phenomenon in hydride/ammonia science: $LiBH_4{\cdot}xNH_3$ becomes liquid-like not simply as the NH_3 content increases, but when Li–N/Li–B coordination-shell mixing is maximized near $x \approx 2$. This mixed-shell regime exhibits weak coordination memory and the broadest sampled Li–N/N···B coordination region, consistent with the liquid-like intermediate. Further ammonia coordination establishes Li–N-dominant coordination and slows BH_4^-/NH_3 contact renewal; the resulting increase in network persistence accompanies re-rigidification. PCI confirms the re-entrant state sequence, while ^1H and ^{11}B NMR capture enhanced mobility at $x = 2$ and recovery of rigidity at $x = 3$, and Raman measurements track the associated local reorganization. Together with the cross-database analysis, these findings identify coordination-shell mixing and network persistence as key determinants of ligand-controlled fluidity and rigidity. This interesting principle may enable transient fluidity for transport and processing, followed by rigidification for structural stability, although its transferability to ammonia-free complex hydrides remains to be tested.

Supplementary Materials

Details of the AI, computational, and experimental methods; Supplementary Figures, Tables, and Discussions.

Data availability

The data that support the findings of this work are included in the published article and its **Supplementary Materials**. Literature-derived experimental and computational records analyzed in this work are available through the Digital Battery platform (*DigBat*: https://www.digbat.org) and Digital Hydrogen platform (*DigHyd*: https://www.dighyd.org). Additional data are available from the corresponding author upon reasonable request.

Acknowledgments

This work was supported by JSPS KAKENHI (Nos. JP25H01508 and JP25K17845) and the JST Strategic International Collaborative Research Program (SICORP; JPMJSC25E2). The authors acknowledge the Center for Computational Materials Science, Institute for Materials Research, Tohoku University for the use of MASAMUNE-IMR (Nos. 202512-SCKXX-0205 and 202512-SCKXX-0218), and the Institute for Solid State Physics (ISSP) at the University of Tokyo for the computational resources.

Reference

1. Mohtadi, R. & Orimo, S. The renaissance of hydrides as energy materials. *Nat Rev Mater* **2**, 16091 **https://doi.org/10.1038/natrevmats.2016.91** (2016).
2. Mohtadi, R., Matsui, M., Arthur, T. S. & Hwang, S. Magnesium borohydride: from hydrogen storage to magnesium battery. *Angew Chem* **124**, 9918–9921 **https://doi.org/10.1002/ange.201204913** (2012).
3. Broom, D. P*., et al.* Hydrogen-based materials for energy storage and conversion. *Nature Reviews Clean Technology* **2**, 512-533 **https://doi.org/10.1038/s44359-026-00184-z** (2026).

4. Zhang, Z. & Nazar, L. F. Exploiting the paddle-wheel mechanism for the design of fast ion conductors. *Nat Rev Mater* **7**, 389–405 **https://doi.org/10.1038/s41578-021-00401-0** (2022).

5. Dematteis, E. M.*, et al.* Hydrogen storage in complex hydrides: past activities and new trends. *Progress in Energy* **4**, 032009 **https://doi.org/10.1088/2516-1083/ac7499** (2022).

6. Le, T.-T., Abbas, M., Dreistadt, D. M., Klassen, T. & Pistidda, C. Ionic conductivity in complex hydrides for energy storage applications: A comprehensive review. *Chem Eng J* **473**, 145315 **https://doi.org/10.1016/j.cej.2023.145315** (2023).

7. Lombardo, L., Nishiguchi, T., Pham, T. H. M., Züttel, A. & Horike, S. Deep Eutectic Solvents Formed by Complex Hydrides: A New Class of Hydrogen-Rich Liquid. *Adv Mater* **37**, 2502566 **https://doi.org/10.1002/adma.202502566** (2025).

8. Züttel, A.*, et al.* Hydrogen storage properties of $LiBH_4$. *J Alloys Compd* **356-357**, 515-520 **https://doi.org/10.1016/S0925-8388(02)01253-7** (2003).

9. Orimo, S.*, et al.* Dehydriding and rehydriding reactions of LiBH4. *J Alloys Compd* **404-406**, 427-430 **https://doi.org/10.1016/j.jallcom.2004.10.091** (2005).

10. Kim, S.*, et al.* A complex hydride lithium superionic conductor for high-energy-density all-solid-state lithium metal batteries. *Nat Commun* **10**, 1081 **https://doi.org/10.1038/s41467-019-09061-9** (2019).

11. Zhang, T.*, et al.* Ammonia, a switch for controlling high ionic conductivity in lithium borohydride ammoniates. *Joule* **2**, 1522–1533 **https://doi.org/10.1016/j.joule.2018.04.015** (2018).

12. Yan, Y.*, et al.* Ammonia-assisted fast Li-ion conductivity in a new hemiammine lithium borohydride, $LiBH_4 \cdot 1/2NH_3$. *Chem Commun* **56**, 3971–3974

https://doi.org/10.1039/C9CC09990E (2020).

13. Johnson, S. R.*, et al.* The monoammoniate of lithium borohydride, $Li(NH_3)BH_4$: an effective ammonia storage compound. *Chemistry–An Asian Journal* **4**, 849-854 **https://doi.org/10.1002/asia.200900051** (2009).

14. Zhang, T., Miyaoka, H., Miyaoka, H., Ichikawa, T. & Kojima, Y. Review on ammonia absorption materials: metal hydrides, halides, and borohydrides. *ACS Applied Energy Materials* **1**, 232-242 **https://doi.org/10.1021/acsaem.7b00111** (2018).

15. Xu, Z.*, et al.* Thermodynamic and spectroscopic analysis of the ammonia absorption mechanism of a borohydride system. *J Mater Chem A* **14**, 5925-5934 **https://doi.org/10.1039/d5ta09030j** (2026).

16. Guo, Y., Xia, G., Zhu, Y., Gao, L. & Yu, X. Hydrogen release from amminelithium borohydride, $LiBH_4{\cdot}NH_3$. *Chem Commun* **46**, 2599-2601 **https://doi.org/10.1039/B924057H** (2010).

17. Zhao, W.*, et al.* Li-Ion conductivity enhancement of $LiBH_4{\cdot}xNH_3$ with *in situ* formed Li_2O nanoparticles. *ACS Appl Mater Interfaces* **13**, 31635-31641 **https://doi.org/10.1021/acsami.1c06164** (2021).

18. Zheng, X.*, et al.* The effect of NH_3 content on hydrogen release from $LiBH_4$–NH_3 system. *Int J Hydrogen Energy* **40**, 4573-4578 **https://doi.org/10.1016/j.ijhydene.2015.01.134** (2015).

19. Sullivan, E. A. & Johnson, S. The lithium borohydride–ammonia system P–C–T relationships and densities. *The Journal of Physical Chemistry* **63**, 233-238 **https://doi.org/10.1021/j150572a024** (1959).

20. Aoki, T., Miyaoka, H., Inokawa, H., Ichikawa, T. & Kojima, Y. Activation on ammonia

absorbing reaction for magnesium chloride. *J Phys Chem C* **119**, 26296-26302 **https://doi.org/10.1021/acs.jpcc.5b07965** (2015).

21. Gao, L., Fang, H., Li, Z., Yu, X. & Fan, K. Liquefaction of solid-state BH_3NH_3 by gaseous NH_3. *Inorg Chem* **50**, 4301-4306 **https://doi.org/10.1021/ic200373g** (2011).

22. Liu, C. Y. & Aika, K.-i. Ammonia absorption into alkaline earth metal halide mixtures as an ammonia storage material. *Ind Eng Chem Res* **43**, 7484-7491 **https://doi.org/10.1021/ie049874a** (2004).

23. Kojima, Y. & Yamaguchi, M. Ammonia storage materials for nitrogen recycling hydrogen and energy carriers. *Int J Hydrogen Energy* **45**, 10233-10246 **https://doi.org/10.1016/j.ijhydene.2020.01.145** (2020).

24. Shen, C., Wang, P., Shen, L., Yin, X. & Miao, Z. NH_3 adsorption performance of silicon-supported metal chlorides. *Ind Eng Chem Res* **61**, 8616-8623 **https://doi.org/10.1021/acs.iecr.2c00916** (2022).

25. Guo, F.*, et al.* Hydrogen carrier by ammonia borane-ammonia system with low-vapor pressure. *Int J Hydrogen Energy* **48**, 27298-27303 **https://doi.org/10.1016/j.ijhydene.2023.03.411** (2023).

26. Kojima, Y. & Yamaguchi, M. Thermodynamic analysis of ammonia storage materials. *Int J Hydrogen Energy* **46**, 11756-11760 **https://doi.org/10.1016/j.ijhydene.2021.01.070** (2021).

27. Aoki, T., Ichikawa, T., Miyaoka, H. & Kojima, Y. Thermodynamics on ammonia absorption of metal halides and borohydrides. *J Phys Chem C* **118**, 18412-18416 **https://doi.org/10.1021/jp5049474** (2014).

28. Iwata, R., Yamauchi, T., Hirota, Y., Aoki, M. & Shimazu, T. Reaction kinetics of ammonia

absorption/desorption of metal salts. *Appl Therm Eng* **72**, 244-249 **https://doi.org/10.1016/j.applthermaleng.2014.07.034** (2014).

29. Smolen, T. M., Manley, D. B. & Poling, B. E. Vapor-liquid equilibrium data for the ammonia-water system and its description with a modified cubic equation of state. *Journal of Chemical and Engineering Data* **36**, 202-208 **https://doi.org/10.1021/je00002a017** (1991).

30. Yang, F., Wang, Q., Cheng, E. J., Zhang, D. & Li, H. User instructions for the Dynamic Database of Solid-State Electrolyte 2.0 (DDSE 2.0). *Computers, Materials and Continua* **81**, 3413-3419 **https://doi.org/10.32604/cmc.2024.060288** (2024).

31. Jang, S.-H.*, et al.* Digital Hydrogen Platform (DigHyd): A rigorously curated database for hydrogen storage materials empowered by AI-assisted literature mining. *arXiv preprint arXiv:260314139*, **https://doi.org/10.48550/arXiv.2603.14139** (2026).

32. Wang, Q.*, et al.* Unraveling the complexity of divalent hydride electrolytes in solid-state batteries *via* a data-driven framework with large language model. *Angew Chem Int Ed* **64**, e202506573 **https://doi.org/10.1002/anie.202506573** (2025).

33. Lyakhov, A. O., Oganov, A. R., Stokes, H. T. & Zhu, Q. New developments in evolutionary structure prediction algorithm USPEX. *Comput Phys Commun* **184**, 1172–1182 **https://doi.org/10.1016/j.cpc.2012.12.009** (2013).

34. Shannon, C. E. A mathematical theory of communications. *Bell system technical journal* **27**, 379-423 **https://doi.org/10.1002/j.1538-7305.1948.tb01338.x** (1948).

35. Laio, A. & Parrinello, M. Escaping free-energy minima. *Proceedings of the National Academy of Sciences* **99**, 12562-12566 **https://doi.org/10.1073/pnas.202427399** (2002).

36. Gao, W.*, et al.* Production of ammonia via a chemical looping process based on metal imides

as nitrogen carriers. *Nat Energy* **3**, 1067-1075 **https://doi.org/10.1038/s41560-018-0268-z** (2018).

37. Wang, Q., *et al.* Ternary ruthenium complex hydrides for ammonia synthesis via the associative mechanism. *Nature Catalysis* **4**, 959-967 **https://doi.org/10.1038/s41929-021-00698-8** (2021).

38. Xiao, Y., *et al.* Electrolyte melt infiltration for scalable manufacturing of inorganic all-solid-state lithium-ion batteries. *Nat Mater* **20**, 984-990 **https://doi.org/10.1038/s41563-021-00943-2** (2021).
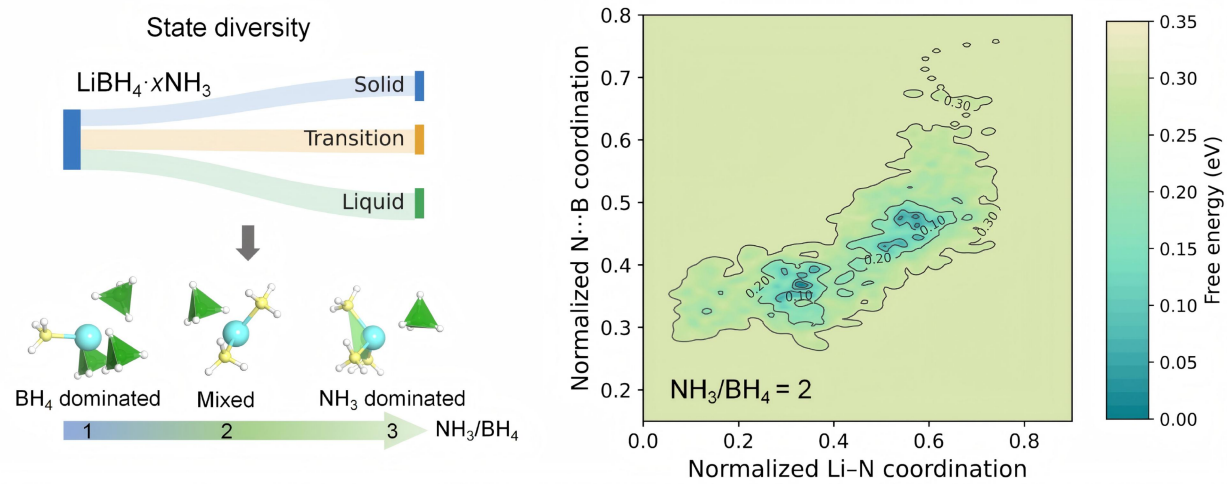
Graphical Abstract